The Dissertation Committee for Ryan Patrick Hannigan certifies that this is the approved version of the following dissertation:

Stranger Things at the LHC

Committee:

Christina Markert, Supervisor

Peter Onyisi

Richard Hazeltine

Chandrajit Bajaj

Stranger Things at the LHC

by

Ryan Patrick Hannigan, B.S.

Dissertation

Presented to the Faculty of the Graduate School of

The University of Texas at Austin

in Partial Fulfillment

of the Requirements

for the degree of

Doctor of Philosophy

The University of Texas at Austin

May, 2023

To Jaynee, who unquestionably is the reason why this document exists.

Stranger Things at the LHC

Publication No. __________________

Ryan Patrick Hannigan, Ph.D.
The University of Texas at Austin, 2023

Supervisor: Christina Markert

Among the most mysterious of the four fundamental forces is the strong nuclear force. Responsible for both the binding together of nucleons within an atom, as well as the

Contents

List of Figures

List of Tables

Chapter One: Introduction

The purpose of this chapter is to transform a scientifically literate reader who may be vaguely familiar with the idea of a "quark" into one who can understand the motivation and techniques behind the analysis presented in the rest of this thesis. If you are an extremely educated physicist who regularly performs lattice quantum chromodynamics calculations in their head, I would also encourage you to read this chapter it its entirety as it may contain egregious errors that need to be corrected.

1.1 What is fundamental?

The answer to the question "What are the fundamental building blocks of our universe?" has changed drastically over the course of human history. The idea that all matter is composed of smaller, uncuttable pieces has been around since 5th century BCE when Greek philosophers Democritus and Leucippus first introduced the concept of an atom [1]. While this idea was mostly motivated by philosophical reasoning, it was later adopted by the English scientist John Dalton in the 19th century to explain the results of his chemical experiments, where he found that chemical elements always combined with each other by discrete units of mass [2]. However, everything changed around the turn of the 20th century when scientists like Rutherford and Chadwick determined that the supposedly indivisible atom was composed of even smaller particles, eventually named protons and neutrons [3], [4]. The notion that protons and neutrons were unbreakable was relatively short lived, as not even half a century later the deep inelastic scattering experiments performed by Kendall, Friedman and Taylor [5]–[7] revealed that protons (and subsequently neutrons) were actually composed of even smaller particles, eventually dubbed "partons". [8]. This discovery was one of the largest contributing factors to the creation of the so-called Standard Model of particle physics, a theory which describes all of the fundamental particles and the way in which they interact with each other. A diagram of those fundamental particles can be seen in Figure 1.1. It should be noted that all of the particles labeled as quarks and leptons – collectively as "fermions" – have corresponding anti-particles with opposite electric charge. The equation that describes all of these

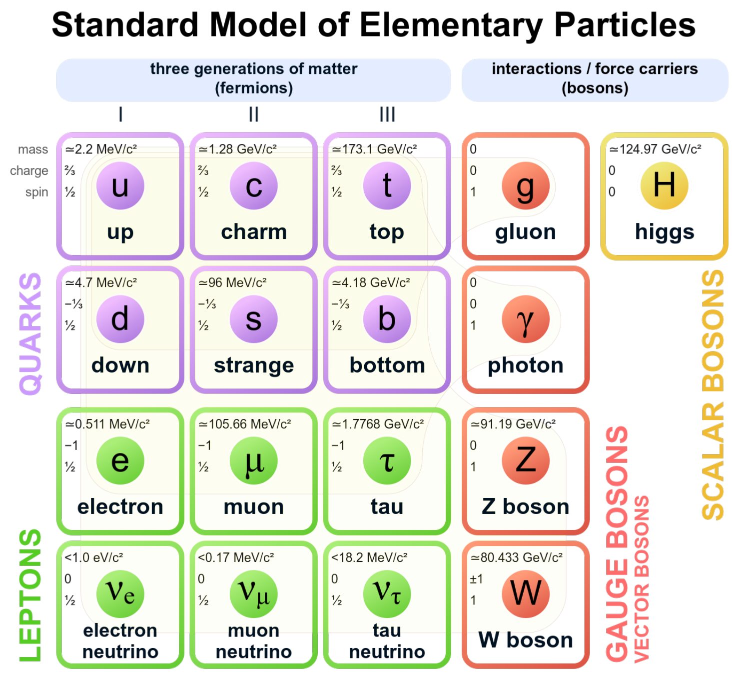

Figure 1.1: A diagram depicting the particles we currently believe are fundamental within the so-called "Standard Model" of particle physics.

particles and their interactions, often incorrectly[1] referred to as the "Standard Model Lagrangian", can be compactified into a relatively palatable form that can easily fit on a coffee cup like the one shown in Figure 1.2.

While this equation may appear brief[1], it can be used to completely describe three of the four fundamental forces of nature:

1. The Electromagnetic Force, which is responsible for the electrons pushing against each other to keep you from falling through your chair,

2. The Weak Nuclear Force, which is responsible for the initiating the nuclear fusion reactions that fuel our sun, and

[1] It is "incorrect" because this is technically a Lagrangian density (i.e. Lagrangian per unit volume), but as it is usually integrated over all space the distinction is mostly irrelevant.

[1] Here "brief" is in the eye of the beholder, but certainly its brevity is misleading as even in the first line the $F_{\mu\nu}$ refers to three completely different gauge field tensors with their indices fully contracted...

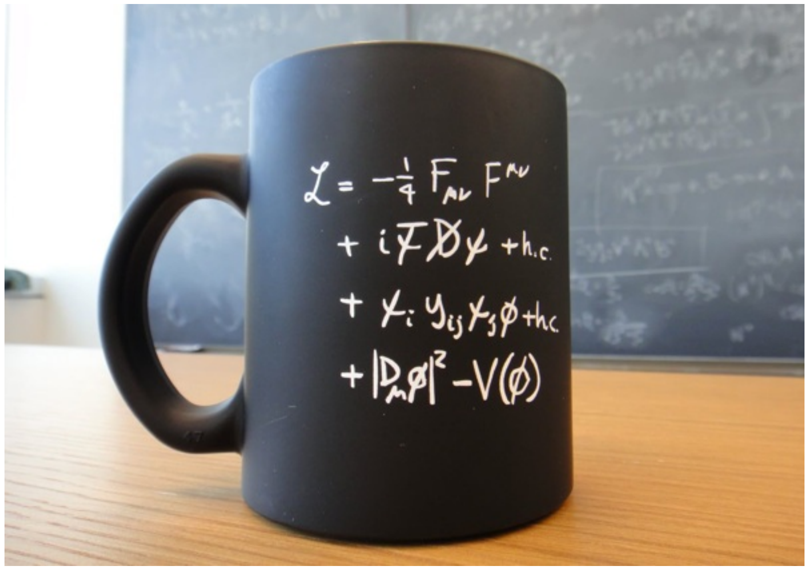

Figure 1.2: A coffee cup with the Standard Model Lagrangian density printed on its side. Please ignore the "+ h.c." term following the $i\bar{\psi}\not{D}\psi$, it is the result of a small lapse in judgement from the mug makers.

3. The Strong Nuclear Force, which is responsible for holding quarks and gluons together in bound stands known as hadrons, like the protons and neutrons that make up everyday matter.

The only fundamental force missing from this list is the Gravitational Force, which is described by a completely separate set of equations[2]

Each of the three forces that are described within the Standard Model are mediated by different gauge bosons. For example, the electromagnetic force is mediated by the boson known as the photon, the weak nuclear force is mediated by the W and Z bosons, and the strong nuclear force is mediated by bosons known as gluons. In this thesis we will be primarily focusing on the Strong Nuclear Force, which acts solely on particles with color charge – an intrinsic property of quarks and gluons. The "color" charges are red, green, and blue with antio

Even though each of the electromagnetic, weak and strong forces can be described using the Standard Model Lagrangian, the way in which they appear within the

[2]Specifically, the Einstein Field Equations, $G_{\mu\nu} + \Lambda g_{\mu\nu} = \kappa T_{\mu\nu}$, but this is the thesis of a particle physicist so gravity is taboo.

equation is not easy to determine. For example, the electromagnetic force actually corresponds to line 1

Chapter Two: Experimental Apparatus

As this thesis is focused on the physics of heavy-ion collisions, it stands to reason that the data analyzed in this thesis was gathered using the only detector along the LHC dedicated to studying such collisions: the ALICE detector. In this chapter, a brief synopsis of the LHC will be provided, followed by a much more detailed overview of the ALICE detector and its corresponding sub-detectors.

2.1 The LHC

Located along the Swiss-French border near Geneva, Switzerland, the Large Hadron Collider (LHC) is the largest particle accelerator on the planet. At a circumference of 27 kilometers, its tunnels lie almost 200 meters beneath the surface of the earth. Inside the tunnels are two high-energy particle beams pointing in opposite directions, with the beam pipes being kept inside of an ultra-high vacuum. The particles inside the beam are guided by a multitude of superconducting magnets: 393 quadrapole magnets keep the beam focused, while 1232 dipole magnets bend the particles along the circular path. The beams are designed to collide at four intersection points along the LHC, each with a corresponding detector surrounding the collision points: (1) ALICE, which specializes in heavy-ion collisions; (2) ATLAS, which specializes in studying high-p_T particles produced in pp collisions, (3) CMS, which TODO and (4) LHCb, which is designed to study CP violations through measurements of B mesons at forward rapidity. A diagram of the LHC with these four intersection points can be seen in Figure 2.1.

Currently, the highest center of mass energies achieved for each of the main collision systems are $\sqrt{s}$ = 13 TeV for pp, $\sqrt{s}$ = 7 TeV for p-Pb and $\sqrt{s}$ = 5.02 TeV for Pb-Pb. The LHC underwent a long shutdown from XXXX to YYYY, in order to upgrade the beam luminosity and COM energies. The projected final COM energies for each collision system will be ...

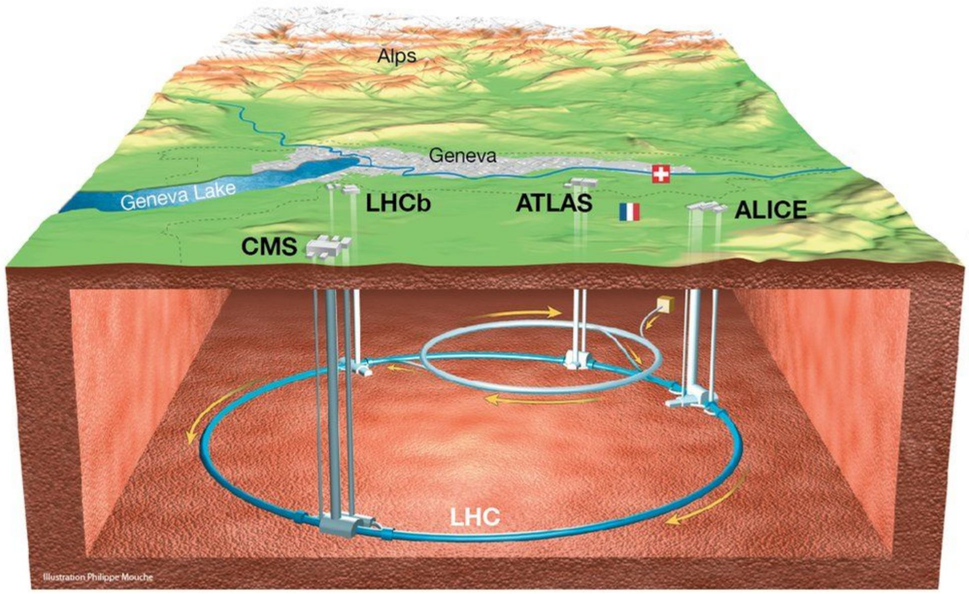

Figure 2.1: A diagram depicting the LHC with its various main detectors shown underground. Illustration by Phillipe Mouche, from BBC News.

2.2 The ALICE Detector

The detector used by the ALICE collaboration, unsurprisingly known as the ALICE detector, has the primary focus of investigating the physical properties of the strongly interacting quark-gluon plasma created during heavy-ion collisions. Building the detector was a massive effort, requiring the help from over 1000 people from 105 institutes in 30 different countries. The detector itself is also massive, weighing in at around 10,000 tons and spanning 26 meters in length with a 16-meter height and width. It is composed of 18 sub-detector systems, all of which work together to help reconstruct the event. A diagram of the detector with its corresponding sub-detector systems can be seen in in Figure 2.2. As the primary focus of the ALICE detector is to study heavy-ion collisions, all of its components must work together to reconstruct very high multiplicity events.

2.2.1 The Inner Tracking System

The Inner Tracking System (ITS) is the inner-most component of the ALICE detector, lying closest to the beam pipe. It is composed of six cylindrical layers of silicon

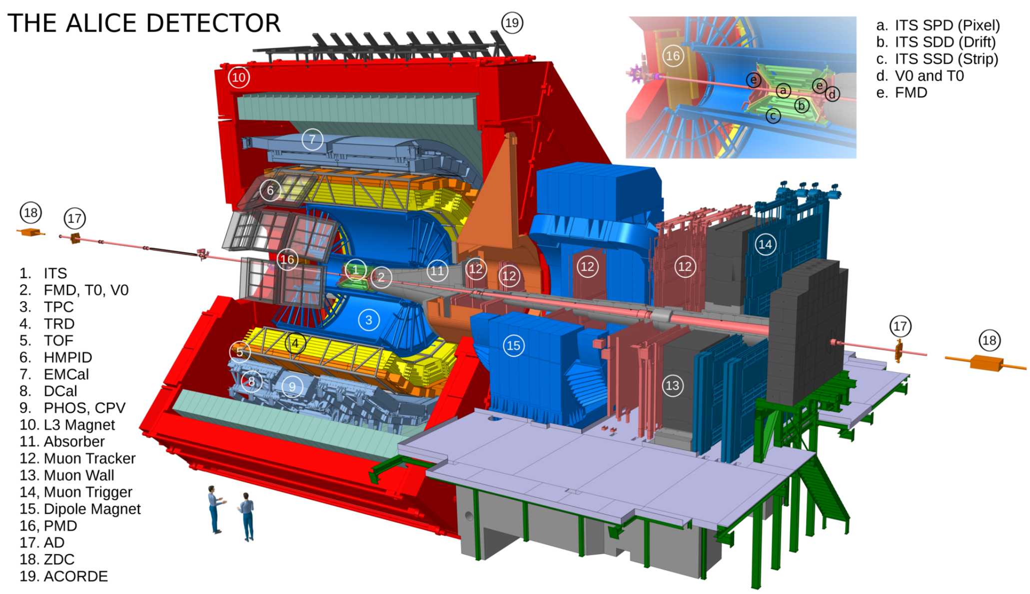

Figure 2.2: A 3-D schematic of the ALICE detector, with labels for all of the sub-detectors. Note the humans-for-scale in the bottom left of the diagram.

detectors that are coaxial with the beam pipe and cover the pseudorapidity range $|\eta| \leq 0.9$. The distance from the beam line varies from 3.9 cm for the first layer to 43 cm for the sixth layer. The ITS uses different types of silicon detectors for each layer: Silicon Pixel Detectors (SPD) for the first and second layers, Silicon Drift Detectors (SDD) for the third and fourth layers, and double sided Silicon Strip Detectors (SSD) for the fifth and sixth layers. Because of its proximity to the interaction point, the ITS is invaluable for reconstructing both primary and secondary vertices and enhancing the tracking capabilities of the ALICE detector near the interaction point. Moreover, the ITS can also track particles that are not detected or missed by the external barrel detector due to acceptance limitations and momentum cutoff.

2.2.1.1 ITS Upgrade

The LHC underwent a fairly substantial upgrade to the beam luminosity from X to Y. In order to utilize all of the The writer of this thesis was the main reason why the ITS Upgrade actually finished, as he is the smartest person of all time and actually hand built the entire thing.

2.2.2 The V0 Detector

V0 is made of two arrays of scintillator counters set on both sides of the ALICE interaction point, and called V0-A and V0-C. The V0-C counter is located upstream of the dimuon arm absorber and cover the spectrometer acceptance while the V0-A counter will be located at around 3.5 m away from the collision vertex, on the other side. It is used to estimate the centrality of the collision by summing up the energy deposited in the two disks of V0. This observable scales directly with the number of primary particles generated in the collision and therefore to the centrality. V0 is also used as reference in Van Der Meer scans that give the size and shape of colliding beams and therefore the luminosity delivered to the experiment.

2.2.3 The Time Projection Chamber

The largest component of the ALICE detector is know nas the Time Projection Chamber (TPC). The TPC is a gas-filled volume with The ALICE Time Projection Chamber (TPC) is a large volume filled with a gas as detection medium and is the main particle tracking device in ALICE.[19][20] Charged particles crossing the gas of the TPC ionize the gas atoms along their path, liberating electrons that drift towards the end plates of the detector. The characteristics of the ionization process caused by fast charged particles passing through a medium can be used for particle identification. The velocity dependence of the ionization strength is connected to the well-known Bethe-Bloch formula, which describes the average energy loss of charged particles through inelastic Coulomb collisions with the atomic electrons of the medium. Multiwire proportional counters or solid-state counters are often used as detection medium, because they provide signals with pulse heights proportional to the ionization strength. An avalanche effect in the vicinity of the anode wires strung in the readout chambers, gives the necessary signal amplification. The positive ions created in the avalanche induce a positive current signal on the pad plane. The readout is performed by the 557 568 pads that form the cathode plane of the multi-wire proportional chambers (MWPC) located at the end plates. This gives the radial distance to the beam and the azimuth. The last coordinate, z along the beam direction, is given by the drift time. Since energy-loss fluctuations can be considerable, in general many pulse-height measurements are performed along the particle track in order to optimize the resolution of the ionization measurement. Almost all of the TPC's volume is sensitive to the traversing charged particles, but it features a minimum material budget. The straightforward pattern recognition (continuous tracks) make TPCs the perfect choice for high-multiplicity environments, such as in heavy-ion collisions, where thousands of particles have to be tracked simultaneously. Inside the ALICE TPC, the ionization strength of all tracks is sampled up to 159 times, resulting in a resolution of the ionization measurement as good as 5

2.2.4 The Electromagnetic Calorimeter

The EMCal is a lead-scintillator sampling calorimeter comprising almost 13,000 individual towers that are grouped into ten super-modules. The towers are read out by wavelength-shifting optical fibers in a shashlik geometry coupled to an avalanche photodiode. The complete EMCal will contain 100,000 individual scintillator tiles and 185 kilometers of optical fiber, weighing in total about 100 tons. The EMCal covers almost the full length of the ALICE Time Projection Chamber and central detector, and a third of its azimuth placed back-to-back with the ALICE Photon Spectrometer – a smaller, highly granular lead-tungstate calorimeter. The super-modules are inserted into an independent support frame situated within the ALICE magnet, between the time-of-flight counters and the magnet coil. The support frame itself is a complex structure: it weighs 20 tons and must support five times its own weight, with a maximum deflection between being empty and being fully loaded of only a couple of centimeters. Installation of the eight-ton super-modules requires a system of rails with a sophisticated insertion device to bridge across to the support structure. The Electro-Magnetic Calorimeter (EM-Cal) will add greatly to the high momentum particle measurement capabilities of ALICE.[26] It will extend ALICE's reach to study jets and other hard processes.

Chapter Three: Analysis Details

This chapter builds upon the analysis overview presented in the previous chapter by providing a much more detailed description of each component of the analysis. These components can be summarized as follows. First, a high-quality data sample of p–Pb collisions is selected, with events further differentiated by their multiplicity. Then, quality tracks are selected for the trigger and associated charged hadrons, and the Λ baryons are reconstructed from lower quality tracks using their characteristic decay topology. These Λ daughter tracks are identified as protons or pions using information from the TPC and TOF detectors. Within a given event, the trigger hadrons are then combined with either the associated charged hadrons or the Λ candidates to form pairs, where a distribution of their relative azimuthal angle ($\Delta\varphi \equiv \varphi_{trig.} - \varphi_{assoc.}$) and pseudorapidity ($\Delta\eta \equiv \eta_{trig.} - \eta_{assoc.}$) is filled for each pair. These h-Λ and h-h angular distributions are then corrected for a laundry list of detector effects using both data- and MonteCaro-driven methods. Further corrections are applied to the h-Λ distributions to account for the combinatorial background associated with the Λ reconstruction and the two-track merging effect, whereby one of the daughter tracks gets merged with the trigger hadron track, causing a h-Λ pair deficit at small angles.

The corrected h-Λ and h-h distributions are then projected onto the $\Delta\varphi$ axis to form 1-dimensional azimuthal correlation distributions. These distributions are used to extract the associated per-trigger yields of Λ baryons and charged hadrons in the near- and away-side of the jet, along with the uncorrelated underlying event (UE). Furthermore, the near- and away-side jet widths are extracted from the h-Λ and h-h $\Delta\varphi$ distributions using a von Mises fitting procedure. These observables are all measured in three event multiplicity percentiles (0-20%, 20-50% and 50-80%) and two associated p_{T} bins ($1.5 < p_{\mathrm{T}}^{\mathrm{assoc.}} < 2.5$ GeV/c and $2.5 < p_{\mathrm{T}}^{\mathrm{assoc.}} < 4.0$ GeV/c).

The structure of this chapter is the following. Section

The systematic uncertainties associated with this analysis are discussed in the next chapter.

3.1 Dataset and event selection

3.1.1 Dataset

Every event in this analysis was a p–Pb collision at $\sqrt{s_{\mathrm{NN}}} = 5.02$ TeV with data collected by the ALICE detector during the 2016 LHC run. This analysis uses the data from these runs with the "FAST" reconstruction, meaning the data was taken without the ITS's SDD subdetector due to issues with readout during this period. The total number of events (prior to any selection) is roughly 400 million. For the the efficiency studies, the analysis was performed using a standard purpose MC-generated production anchored to the dataset using the DPMJET [9] event generator. This production consists of around 400 million minimum bias events, which is roughly equivalent to data.

3.1.2 Event Selection

Events are selected by requiring the location of the primary collision interaction point (called the "primary vertex" or PV) to be no more than 10 cm from the center of the detector along the beam axis or "z"-direction. Furthermore, every event is required to have at least three reconstructed tracks that contributed to the reconstruction of the PV. This reduces the total number of events considered to approximately 350 million events, and a summary of the effects of these selection criteria can be seen in Table 3.1. The events are further separated into three charged particle multiplicity classes (0-20%, 20-50% and 50-80%) based off event activity in the forward-rapidity V0A detector.

Table 3.1: Number of events passing our criteria for each multiplicity bin considered. Here Z_{vtx} refers to the position of the PV along the beam (z) axis.

Multiplicity	Total evts.	Has 3 tracks	$\|Z_{vtx}\| < 10$cm + 3 tracks	% Pass
0-20%	1.0E08	1.0E08	0.8E08	87%
20-50%	1.6E08	1.6E08	1.3E08	86%
50-80%	1.6E08	1.6E08	1.3E08	86%

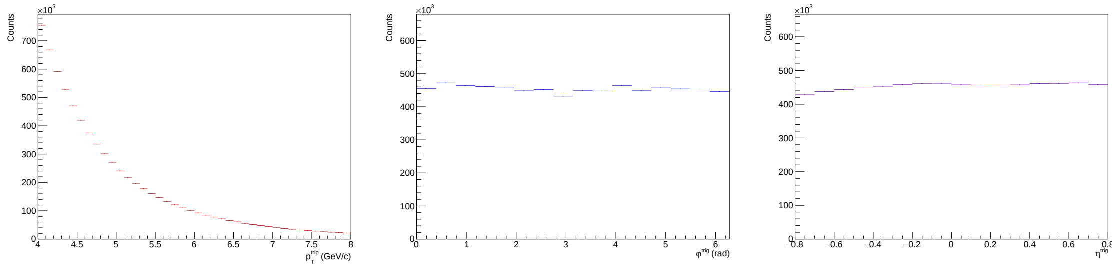

Figure 3.1: The p_{T} (left), φ (middle) and η (right) distributions for the trigger hadrons in the multiplicity range 0-20%.

3.2 Charged hadron track selection

3.2.1 Trigger track cuts

For any two-particle correlation analysis, the selection criteria of the trigger hadron is of utmost importance as any geometric biases introduced by the trigger selection could be reflected in the final correlation distributions. However, correlation analyses generally require large statistics, thus the selection criteria shown in Table 3.2 are applied to ensure the quality of the trigger hadron track while maximizing the statistics of the analysis. Furthermore, the trigger hadron tracks are required to be at midrapidity ($|\eta| < 0.8$) and have high[1] momentum with $4.0 < p_{\mathrm{T}}^{\mathrm{trig.}} < 8.0$ GeV/c, as the trigger is meant to serve as a proxy for a jet axis. Plots of the p_{T}, φ and η distributions for the trigger hadrons that pass these cuts in the 0-20% multiplicity bin can be seen in Figure 3.1.

Table 3.2: The track quality cuts applied to the trigger hadrons in this analysis.

Selection criterion	Value
TPC clusters	≥ 50
χ^2 per TPC cluster	< 4
Fraction of shared TPC clusters	< 0.4
DCA$_{xy}$	< 2.4 cm
DCA$_z$	< 3.2 cm
Accept kink daughters	No

[1] "High" in this case means high enough to guarantee the hadron is produced close (in $\Delta\varphi\Delta\eta$-space) to a jet axis.

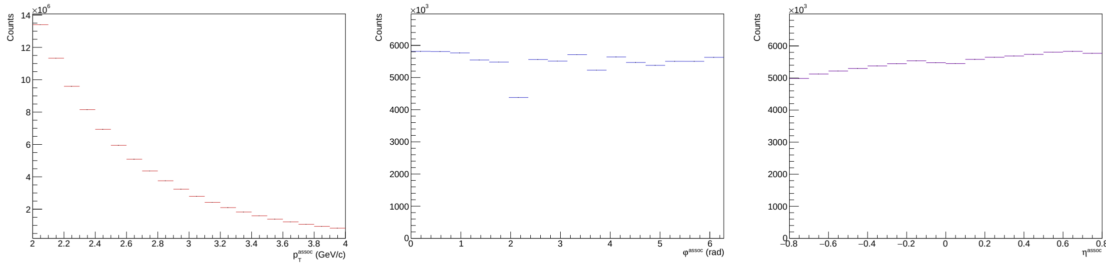

Figure 3.2: The p_{T} (left), φ (middle) and η (right) distributions for the associated hadrons in the multiplicity range 0-20%. The dips observed in the φ distribution are due to the TPC sector boundaries.

3.2.2 Associated hadron track cuts

To keep the results of this analysis more comparabile to previous measurements of the $\Lambda/\pi \approx \Lambda/\mathrm{h}$ ratio, the selection criteria for the associated hadrons are more strict than those for the trigger hadrons as the associated hadrons are meant to be "primary", meaning they did not originate from a weak decay. All associated hadrons are required to meet the ALICE standard track quality cuts for primary charged hadrons described in Table 3.3. Furthermore, the associated hadrons are selected only at midrapidity ($|eta| < 0.8$) in the momentum region $1.0 < p_{\mathrm{T}} < 4.0\mathrm{GeV}/c$, with further binning performed offline. The p_{T}, φ and η distributions for the associated hadrons that pass these cuts in the 0-20% multiplicity bin can be seen in Figure 3.2.

Table 3.3: The ALICE standard track quality cuts for primary charged hadrons, used for the selection of the associated hadrons in this analysis.

Selection criterion	Value
Crossed rows in TPC	≥ 80
Crossed rows/findable clusters in TPC	> 0.8
TPC clusters	≥ 80
ITS clusters	≥ 3
χ^2 per TPC cluster	< 4
χ^2 per ITS cluster	< 36
TPC and ITS refit required	Yes
DCA_{xy}	$< 0.0105 + 0.0350/p_{\mathrm{T}}^{1.1}$ cm
DCA_z	< 2 cm

3.3 Λ reconstruction

3.3.1 Characteristic V^0 decay topology

The Λ candidates in this analysis are reconstructed using their characteristic "V"-shaped decay topology, which is seen in the detector as two oppositely charged tracks originating from a common vertex which is sufficiently displaced from the PV (called the "secondary vertex" or SV). Such particles capable of being reconstructed via this topology are called "V^0"s: the V describing the decay shape and the 0 indicating that the particle is neutral. A diagram depicting a typical V^0 decay is shown in Figure 3.3, with labels given for the most relevant kinematic variables.

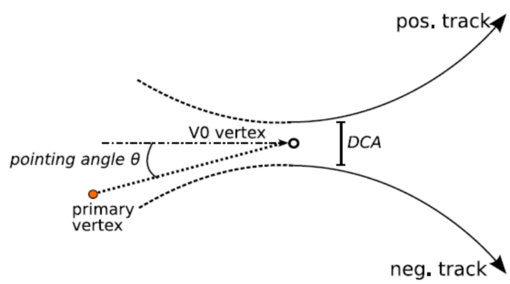

Figure 3.3: A diagram depicting a typical V^0 decay with labels for the most important kinematic variables. The diagram was taken from [10].

The first and most important of these variables is the distance of closest approach (DCA) between the two tracks. This DCA needs to be small enough (relative to the tracking resolution) to ensure that the tracks originated from a common vertex. Another important variable is the transverse decay length of the V^0, which is the distance between the PV and the SV measured in the xy-plane. The importance of this variable is twofold: if the decay length is too small, then it may not even be possible to resolve the SV from the PV, plus it allows for the distinction between V^0s of differing decay lengths. The final relevant variable is the cosine of the pointing angle, which is the angle between the momentum vector of the V^0 and the vector pointing from the PV to the SV. As V^0 candidates are generally required to be sufficiently collimated to ensure that the V^0 originated from the PV, the cosine of the pointing angle is usually close to unity.

Using these variables, a list of likely V^0 candidates is generated for each event, from which further cuts are applied to maximize the likelihood of the candidate being a true Λ baryon. These cuts are summarized in the following section. There is also another technique for Λ reconstruction whereby all oppositely charged proton-pion pairs are combined to form Λ candidates, which is explored in more detail in Chapter **??**. However, due to the large combinatorial background associated with this technique, the V^0 method described above is nominal for this analysis.

3.3.2 Λ daughter proton and pion track cuts

Because of the longer decay length of the Λ ($c\tau \approx 10$ cm), the corresponding daughter proton and pion tracks generally have fewer hits in both the ITS and TPC, resulting in "lower quality" track parameters. Because of this, the cuts applied to the daughter tracks used to reconstruct Λ candidates are the least strict of all the track quality cuts in this analysis and are summarized in Table 3.4. The daughter proton and pion are also required to be at midrapidity ($|\eta| < 0.8$) and have a minimum p_{T} of $p_{\mathrm{T}} > 0.15$ GeV/c.

Table 3.4: The track quality cuts applied to both the daughter proton and pion tracks used to reconstruct Λ candidates. These cuts are intentionally less strict than those applied to the trigger and associated hadrons as the daughter tracks are reconstructed from secondary particles.

Selection criterion	Value
TPC refit required	Yes
Crossed rows in TPC	≥ 70
Crossed rows/findable clusters in TPC	> 0.8

Following the particle identification procedure outlined in Sections **??** and **??**, the daughter proton and pion tracks are required to pass the following PID cuts using both the TPC and TOF detectors:

- $|n\sigma_{\mathrm{TPC},p}| < 2$
- $|n\sigma_{\mathrm{TPC},\pi}| < 3$
- $|n\sigma_{\mathrm{TOF},p}| < 2$ (if signal exists)
- $|n\sigma_{\mathrm{TOF},\pi}| < 3$ (if signal exists)

The values of these cuts were chosen to maximize the Λ signal while avoiding contamination from other particle species. The parenthetical "if signal exists" means that the TOF PID cut is only applied if the track has a TOF signal. Due to the large distance between the TOF detector and the PV, many lower momentum tracks are deflected by the magnetic field before reaching the TOF detector, resulting in no signal. Excluding such tracks results in a more pure sample of protons and pions, at the cost of a much lower number of Λ candidates. While such a cost is not acceptable for the nominal analysis, the effect of excluding these tracks is investigated in Chapter **??**. The $n\sigma$ distributions for both the TPC and TOF detectors of the daughter proton and pion tracks that pass the aforementioned quality cuts are shown in Figure 3.4 and Figure 3.5, respectively. To check for contamination from other particle species, the TOF and TPC information is combined to form a $n\sigma_{\text{TOF}}$ vs $n\sigma_{\text{TPC}}$ plot, which is shown for both the protons and pions in Figure 3.6. No contamination is observed for either the proton or pion tracks.

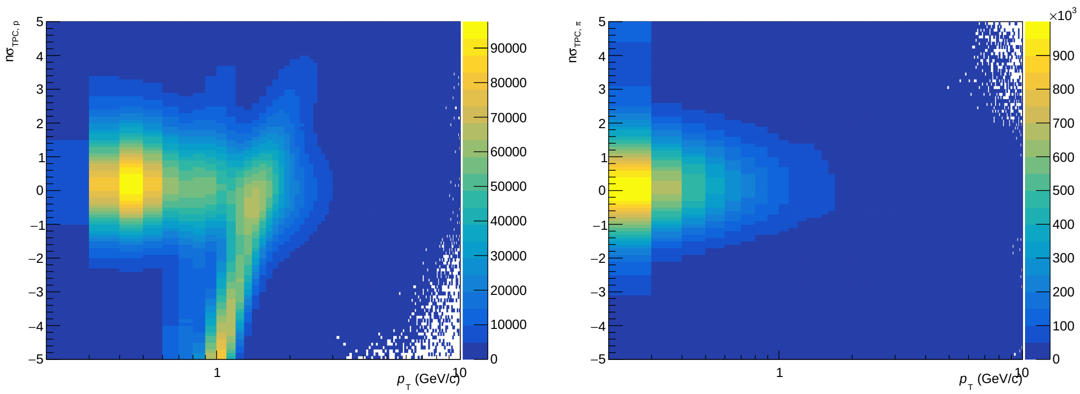

Figure 3.4: $n\sigma$ for protons (left) and pions (right) in the TPC detector as a function of p_T.

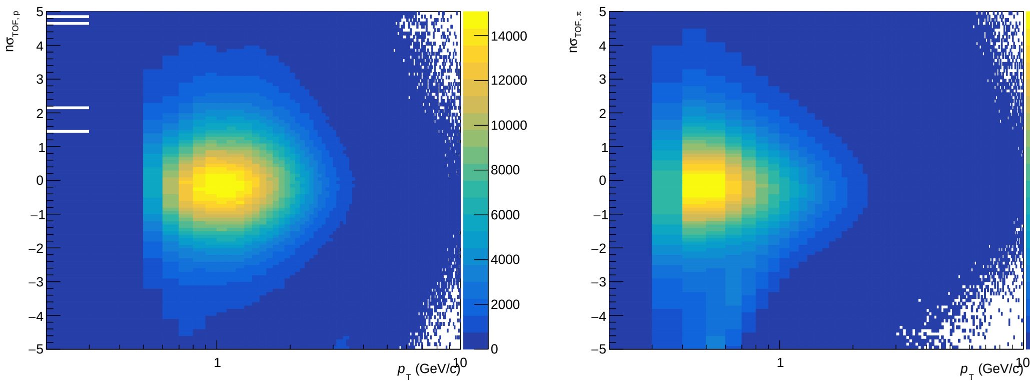

Figure 3.5: $n\sigma$ for protons (left) and pions (right) in the TOF detector as a function of p_T.

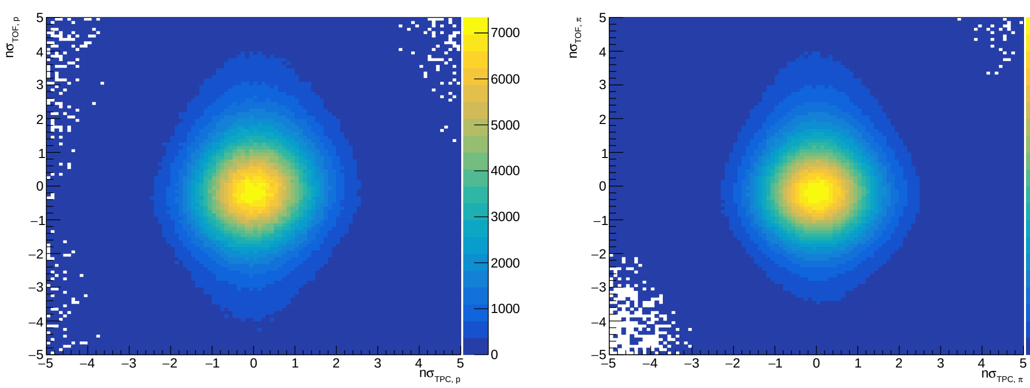

Figure 3.6: $n\sigma$ in TOF vs $n\sigma$ in TPC for protons (left) and pions (right). No contimatination is observed for both of the particle species.

3.3.3 Λ candidate selection

With the daughter proton and pion tracks selected, the Λ candidates are generated by combining all oppositely charged proton-pion pairs into V^0s which meet the topological selection criteria described in Table 3.5.

Table 3.5: Topological selection criteria applied to Λ candidates.

Selection criterion	Value
$\lvert\eta\rvert$	< 0.8
Decay radius (cm)	> 0.2
DCA_{xy} of pion track to PV (cm)	> 0.06
DCA_{xy} of proton track to PV (cm)	> 0.06
DCA_{xy} between daughter tracks (nσ)	< 1.5
$\cos(\theta_{\mathrm{pointing}})$	> 0.9
Invariant mass (GeV/c^2)	$1.102 < M_{p\pi} < 1.130$

The invariant mass $M_{p\pi}$ is calculated using

$$M_{p\pi} = \sqrt{(E_p + E_\pi)^2 - (\vec{p}_p + \vec{p}_\pi)^2}, \tag{3.1}$$

where $E_x = \sqrt{m_x^2 + p_x^2}$ is the energy of the particle of species x. The $M_{p\pi}$ distributions for the Λ candidates for all multiplicity and momentum bins are shown in Figure 3.7. The distributions are also fit with a Voigtian function (convolution of Breit-Wigner and Gaussian [11]) plus a straight line to describe the background. Note that despite our selection criteria, there is still a non-negligible background due to the presence of misidentified Λ candidates. As this background inevitably makes its way into the final h-Λ correlation distributions, it is removed using the technique described in Section **??**.

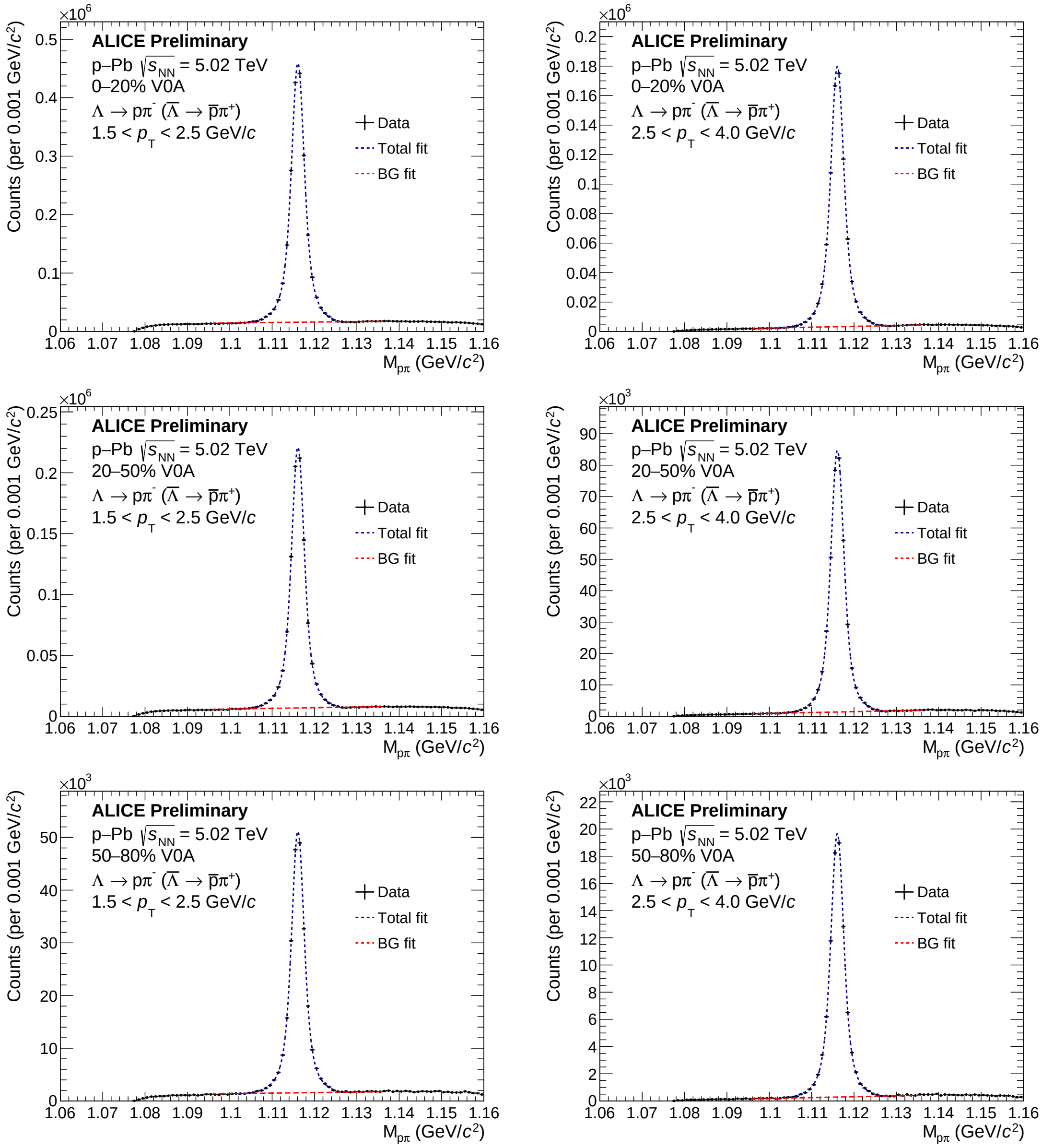

Figure 3.7: Invariant mass distributions in the 0-20% (top), 20-50% (middle), and 50-80% (bottom) multiplicity bins for the Λ candidates which pass the selection criteria with $1.5 < p_{\mathrm{T}} < 2.5$ GeV/c (left) and $2.5 < p_{\mathrm{T}} < 4.0$ GeV/c (right). A Voigtian signal + straight-line background fit to the data is shown in blue, with just the background fit shown in red. For these plots, the Λs were only reconstructed in events with a trigger hadron.

3.4 Reconstruction efficiency

In an ideal world, the number of reconstructed particles of interest would be equal to the number of particles produced in the collision. Unfortunately this is not the case, as there are a number of detector effects which can cause particles to be "lost" during reconstruction. To correct for these effects, the reconstruction efficiency

$$\epsilon(x_1, x_2, ..., x_n) \equiv P(f(x_1, x_2, ..., x_n)|g(x_1, x_2, ..., x_n)), \tag{3.2}$$

is used. Here x_i are the kinematic variables of the particle of interest (e.g. p_{T}, η, φ), $f(x_1, x_2, ..., x_n)$ is the probability that a particle is reconstructed ("found") with kinematic variables x_i, and $g(x_1, x_2, ..., x_n)$ is the probability that a particle is produced ("generated") with the same variables. While the distributions f and g are inaccessable within a given event, the efficiency can be calculated using Monte Carlo simulation techniques via the equation

$$\epsilon(x_1, x_2, ..., x_n) = \frac{N_{\mathrm{reco.}}(x_1, x_2, ..., x_n)}{N_{\mathrm{gen.}}(x_1, x_2, ..., x_n)}, \tag{3.3}$$

where $N_{\mathrm{reco.}}$ and $N_{\mathrm{gen.}}$ are the reconstructed and generated particle distributions, respectively, usually taken across a large number of simulated events. In this analysis, these distributions are calculated as a function of p_{T} and η for each multiplicity class using 30 million events generated by the Monte Carlo event generator DPMJET [9] with particle propagation through the ALICE detector performed by the GEANT3 [12] detector simulation software. These efficiency distributions are then used to correct the h-Λ and h-h correlation distributions using the procedure described in Section 3.5.

3.4.1 Charged hadron reconstruction efficiency

The trigger and associated hadron track reconstruction efficiencies are calculated using Equation 3.3, where the trigger and associated hadrons from $N_{\mathrm{reco.}}$ are subject to the following:

- The track passes the quality cuts outlined in Tables 3.2 (trigger) or 3.3 (associated)

- The track has a corresponding generated particle

- That generated particle is either a pion, proton, kaon, electron or muon
- $|\eta_{\text{track}}| \leq 0.8$,

and the trigger and associated hadrons from $N_{\text{gen.}}$ are subject to:

- $|\eta_{\text{track}}| \leq 0.8$
- The particle is either a pion, proton, kaon, electron or muon
- The particle is primary (i.e. did not originate from a weak decay)

The trigger and associated track reconstruction efficiencies are shown for each multiplicity class as a function of p_{T} in Figure 3.8. While these efficiencies exhibit relatively flat behavior as a function of p_{T} and multiplicity, they are still treated as p_{T} and multiplicity dependent during the correction procedure.

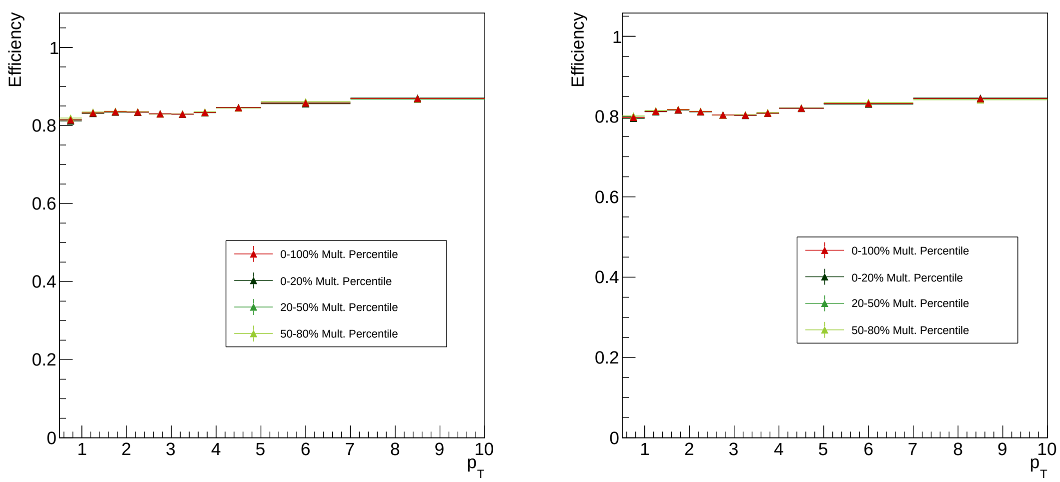

Figure 3.8: Efficiency vs. p_T for trigger (left) and associated (right) hadrons. While they may look identical, the associated hadron efficiency is slightly lower due to the stricter selection criteria.

3.4.2 Λ reconstruction efficiency

The Λ reconstruction efficiency is calculated as a function of p_{T} and η using Equation 3.3, where the Λs from $N_{\text{reco.}}$ are subject to the following:

- They pass the topological selection criteria from Table 3.5
- The reconstructed daughter p, π tracks pass the quality cuts from Table 3.4
- The daughter p, π tracks have corresponding generated p, π particles
- Those generated p, π daughters come from the same mother Λ
- $|\eta_\Lambda| \leq 0.8$,

and the Λs from $N_{\text{gen.}}$ are subject to:

- $|\eta_\Lambda| \leq 0.8$
- The Λ decays to pπ.

The requirement that the generated Λs decay into pπ means the branching ratio is not included in the efficiency calculation as it is corrected for separately (see Section 3.5). The Λ reconstruction efficiency can be seen for each multiplicity class as a function of p_{T} and η in Figure 3.9. Note that the efficiency is no longer flat as a function of η due to the $|\eta| < 0.8$ requirement for the daughter tracks, which kinematically restricts the Λ reconstruction to a smaller η range.

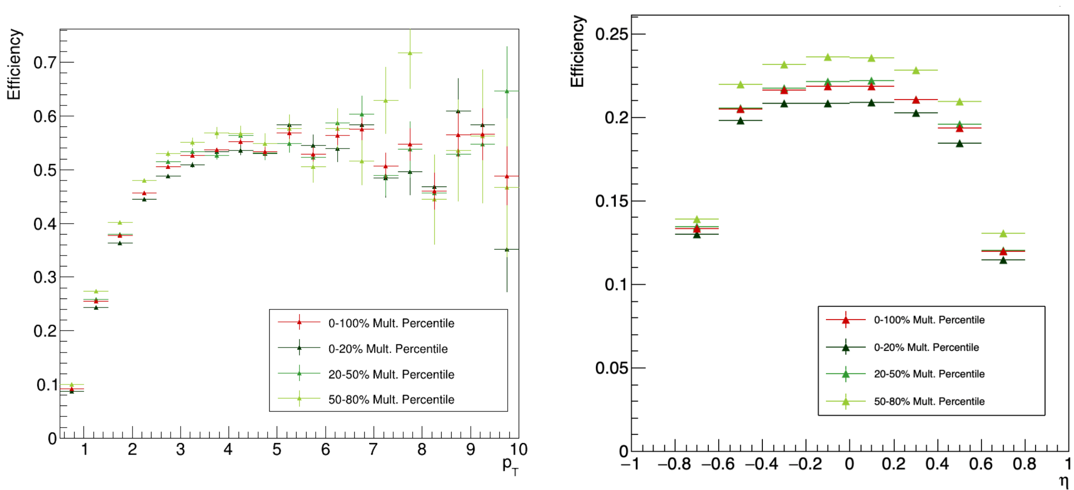

Figure 3.9: Efficiency vs. p_T (left) and η (right) for Λ reconstruction in each multiplicty bin, along with an integrated 0-100% point in red.

3.5 Corrections to the correlation distributions

Once the trigger and associated particles are selected, the two-particle h-Λ and h-h correlation distributions are generated. As mentioned in the previous chapter, the corrected two-particle correlation function is given by

$$\frac{1}{N_{trig}}\frac{d^2N_{pair}}{d\Delta\varphi d\Delta\eta} = \frac{1}{N_{trig}^{corr}}\frac{1}{\epsilon_{trig}\times\epsilon_{assoc}}B(0,0)\frac{S(\Delta\varphi,\Delta\eta)}{B(\Delta\varphi,\Delta\eta)}\frac{1}{\epsilon_{pair}(\Delta\varphi,\Delta\eta)}. \tag{3.4}$$

which contains a number of explicit correction terms (in the form of ϵs) along with some implicit corrections. These corrections are described in this section, and are presented in the order in which they are applied to the data.

3.5.1 Single-particle efficiency corrections

As both the trigger and the associated particles have their own independent reconstruction efficiencies, the trigger-associated pair reconstruction efficiency should be

$$\epsilon_{\text{trig,assoc}} = \epsilon_{\text{trig}} \times \epsilon_{\text{assoc}}, \tag{3.5}$$

meaning the single-particle efficiency distributions from Section 3.4 can be used to calculate the weight $1/(\epsilon_{trig} \times \epsilon_{assoc})$. This weight is applied for each h-Λ and h-h pair in the two-dimensional correlation distribution. However, the assumption that the reconstruction efficiencies are independent is slightly incorrect in the case of the h-Λ distributions due to track merging effects, thus an additional ϵ_{pair} correction is required (discussed in detail in Section **??**).

The trigger efficiency weight $1/\epsilon_{trig}$ is also applied to the single-particle trigger hadron distribution in data to obtain N_{trig}^{corr}.

3.5.2 Mixed-event acceptance correction

As mentioned in Section **??**, the $B(0,0)/B(\Delta\varphi,\Delta\eta)$ term in Equation 3.4 corrects for the finite acceptance along η as both our trigger and associated particles are required to be within $|\eta| < 0.8$. The mixed-event distribution $B(\Delta\varphi,\Delta\eta)$ shown in Figure **??** has a characteristic triangular shape along $\Delta\eta$, which is purely due to detector geometry as no physical correlations are present. When scaled by $1/B(0,0)$, the mixed event distribution becomes the probability that a particle pair is found given that the trigger particle is within $|\eta| < 0.8$, which is unity at $\Delta\varphi, \Delta\eta = 0, 0$. Thus correcting the same-event distribution $S(\Delta\varphi, \Delta\eta)$ by $B(0,0)/B(\Delta\varphi, \Delta\eta)$ removes this acceptance effect and allows for a more accurate determination of the pair-wise yields.

While the generation of the mixed event distribution $B(\Delta\varphi, \Delta\eta)$ was discussed briefly in Section **??**, the specific details are as follows. First, in order to ensure that the mixed-event pairs are coming from similar events, the events in the mixing pool are separated by both multiplicity percentile and $Z_{\text{vtx.}}$ position. The categorizing of events based off of $Z_{\text{vtx.}}$ position is an integral part of the acceptance correction: events with a $Z_{\text{vtx.}}$ at one edge of the detector have a completely different (and nearly inverted) η acceptance than those on the opposite edge. The multiplicity bins are the same as they are for the same-event distributions (namely 0-20%, 20-50% and 50-80%), and the ten $Z_{\text{vtx.}}$ bins are split evenly from -10 cm to 10 cm. For each multiplicity and $Z_{\text{vtx.}}$ bin, the acceptance correction

$$S_{\text{corr.}}(\Delta\varphi, \Delta\eta) = \frac{S(\Delta\varphi, \Delta\eta)}{B(\Delta\varphi, \Delta\eta)/B(0,0)} \tag{3.6}$$

is performed, and the results for each multiplicity bin are then merged across all $Z_{\text{vtx.}}$ bins. The uncorrected distributions $S(\Delta\varphi, \Delta\eta)$ and the mixed-event distributions $B(\Delta\varphi, \Delta\eta)$ are shown for both the h-Λ and h-h cases for all multiplicity and associated momentum bins in Figures 3.10 through 3.13.

This mixed-event correction is the final correction applied to the h-h distributions. However, the h-Λ distributions require additional corrections that are not present in the dihadron case.

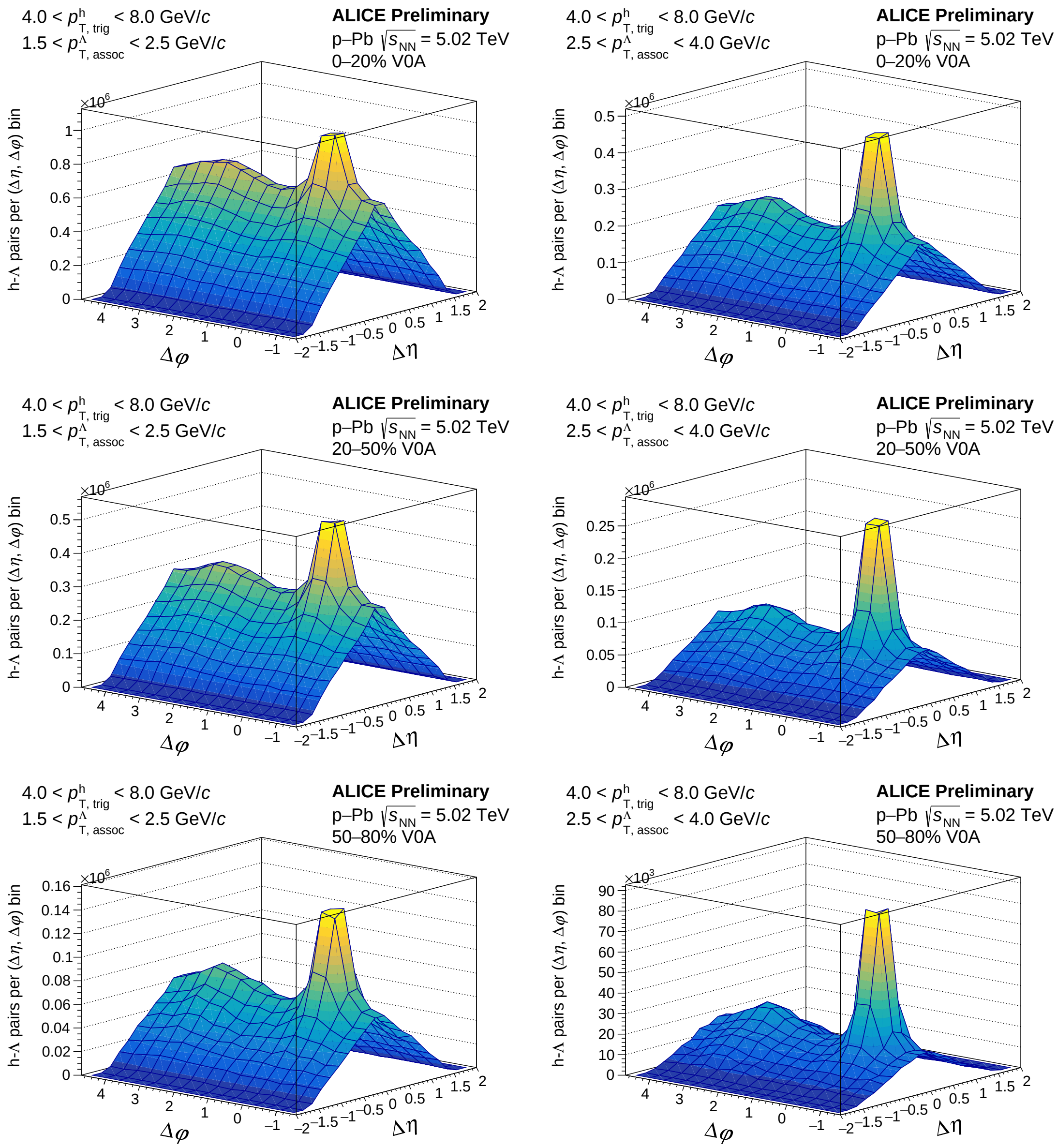

Figure 3.10: 2-D non-acceptance corrected h-Λ angular correlations for the 0-20% (top), 20-50% (middle), and 50-80% (bottom) multiplicity bins for $1.5 < p_{\mathrm{T}} < 2.5$ GeV/c (left) and $2.5 < p_{\mathrm{T}} < 4.0$ GeV/c (right).

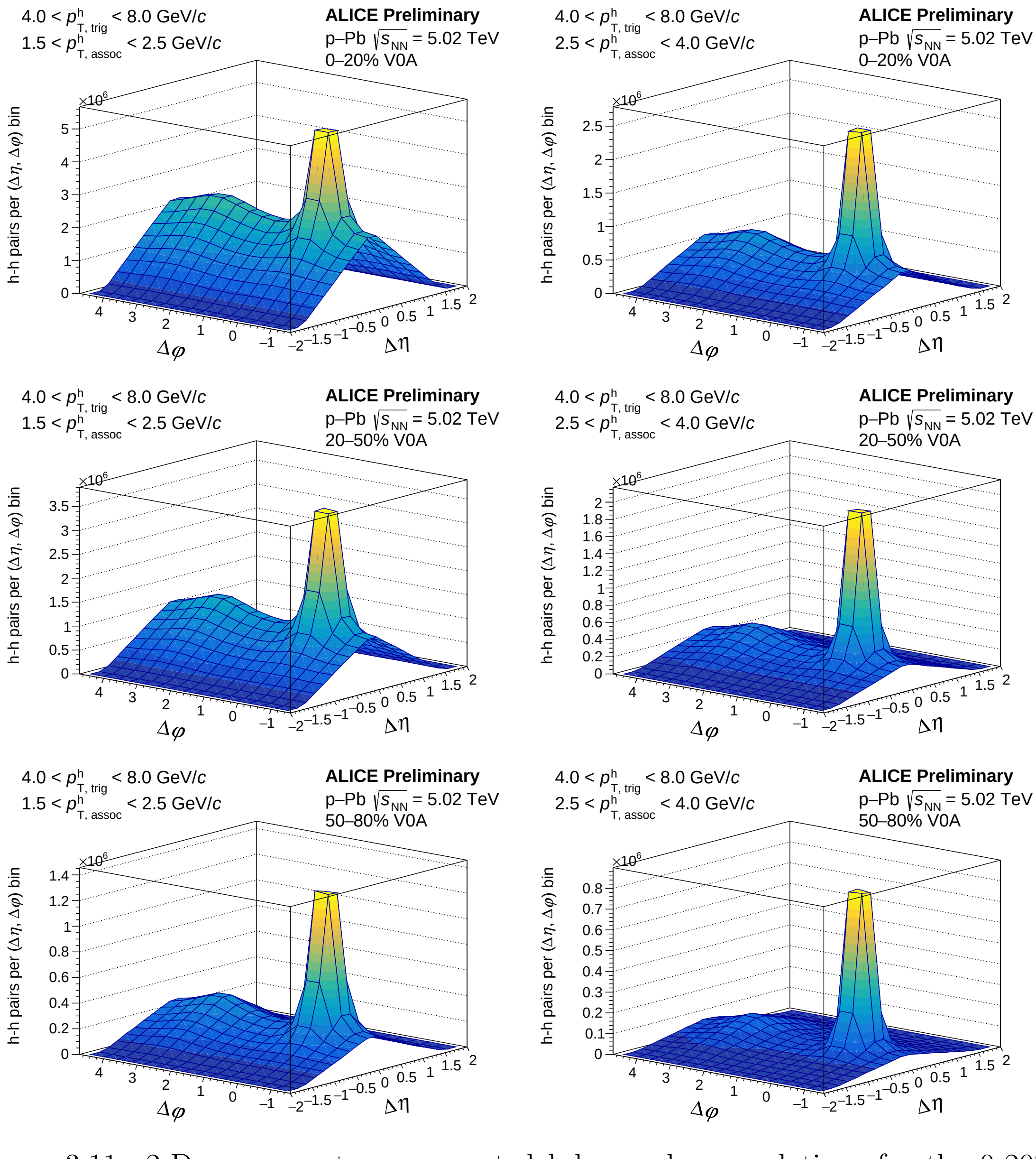

Figure 3.11: 2-D non-acceptance corrected h-h angular correlations for the 0-20% (top), 20-50% (middle), and 50-80% (bottom) multiplicity bins for $1.5 < p_{\mathrm{T}} < 2.5$ GeV/c (left) and $2.5 < p_{\mathrm{T}} < 4.0$ GeV/c (right).

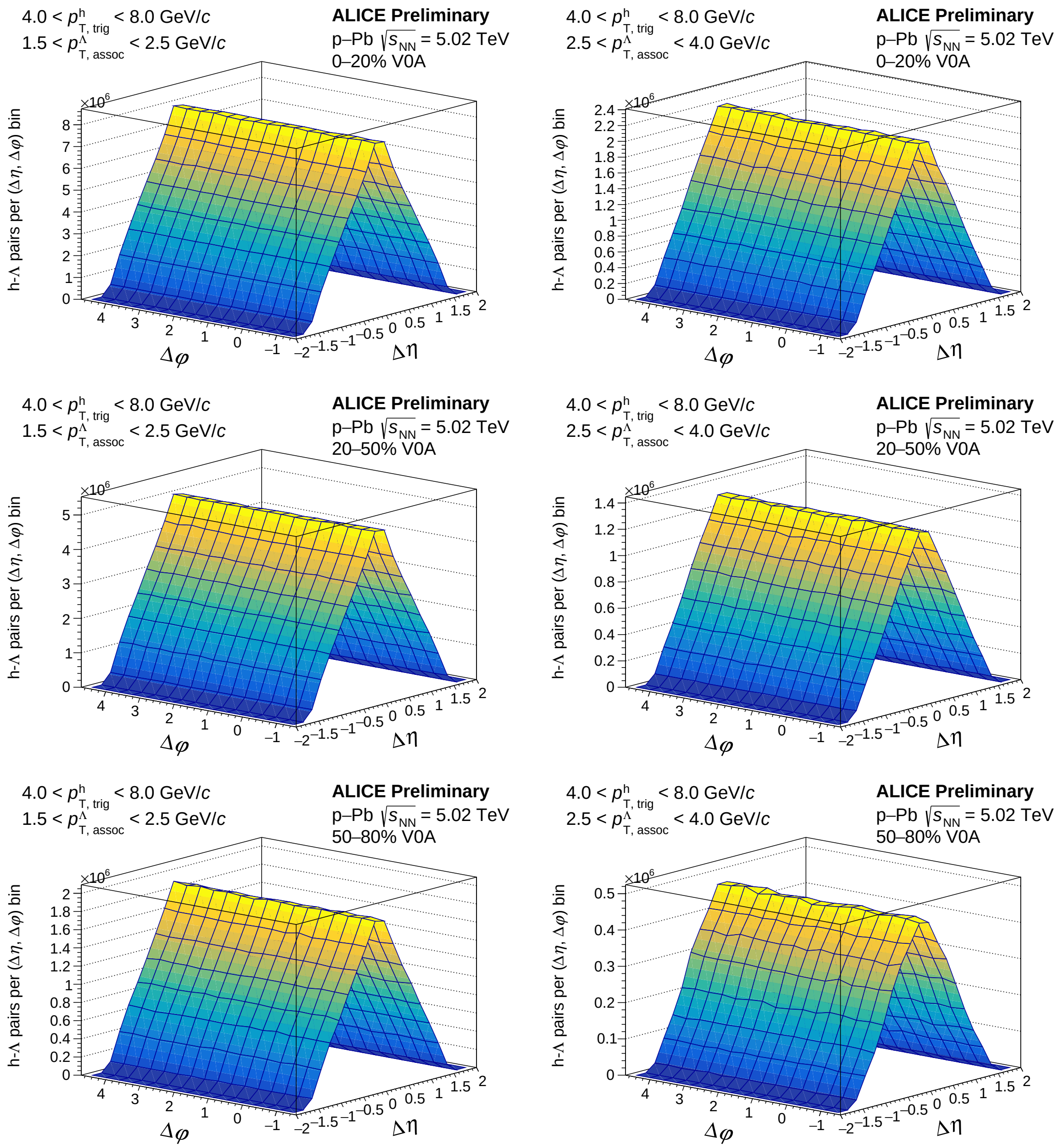

Figure 3.12: 2-D mixed-event h-Λ angular correlations for the 0-20% (top), 20-50% (middle), and 50-80% (bottom) multiplicity bins for $1.5 < p_{\mathrm{T}} < 2.5$ GeV/c (left) and $2.5 < p_{\mathrm{T}} < 4.0$ GeV/c (right). The $Z_{\mathrm{vtx.}}$ bins are merged together for these plots.

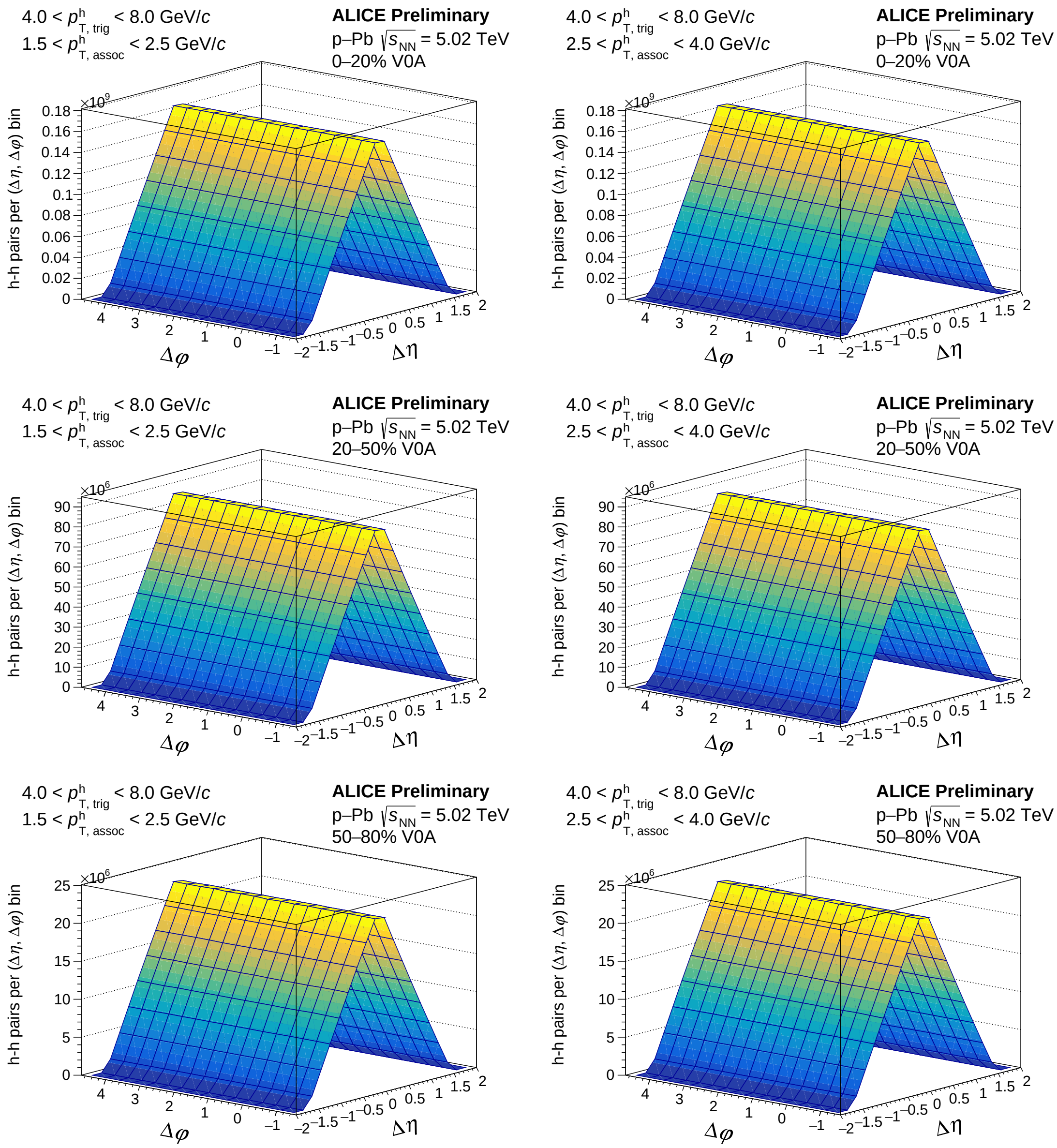

Figure 3.13: 2-D mixed-event h-h angular correlations for the 0-20% (top), 20-50% (middle), and 50-80% (bottom) multiplicity bins for $1.5 < p_{\mathrm{T}} < 2.5$ GeV/c (left) and $2.5 < p_{\mathrm{T}} < 4.0$ GeV/c (right). The $Z_{\mathrm{vtx.}}$ bins are merged together for these plots.

Bibliography

[1] B. Pullman, *The Atom in the History of Human Thought*. Oxford: Oxford University Press, 1998, ISBN: 978-0-19-515040-7 (cit. on p. 1).

[2] J. Dalton, "Experimental enquiry into the proportion of the several gases or elastic fluids, constituting the atmosphere," *Memoirs of the Literary and Philosophical Society of Manchester*, vol. 1, pp. 244–258, 1805 (cit. on p. 1).

[3] E. Rutherford, "The scattering of α and β particles by matter and the structure of the atom," *Philosophical Magazine Series 6*, vol. 21, pp. 669–688, 1911 (cit. on p. 1).

[4] J. Chadwick, "Possible existence of a neutron," *Nature*, vol. 129, p. 312, 1932 (cit. on p. 1).

[5] H. Kendall, *Deep inelastic scattering: Experiments on the proton and the observation of scaling*, 1990. [Online]. Available: `https://www.nobelprize.org/uploads/2018/06/kendall-lecture.pdf` (visited on 08/21/2023) (cit. on p. 1).

[6] J. Friedman, *Deep inelastic scattering: Comparisons with the quark model*, 1990. [Online]. Available: `https://www.nobelprize.org/uploads/2018/06/friedman-lecture.pdf` (visited on 08/21/2023) (cit. on p. 1).

[7] R. Taylor, *Deep inelastic scattering: The early years*, 1990. [Online]. Available: `https://www.nobelprize.org/uploads/2018/06/taylor-lecture.pdf` (visited on 08/21/2023) (cit. on p. 1).

[8] R. P. Feynman, "The behavior of hadron collisions at extreme energies," in *Special Relativity and Quantum Theory: A Collection of Papers on the Poincaré Group*, M. E. Noz and Y. S. Kim, Eds. Dordrecht: Springer Netherlands, 1988, pp. 289–304, ISBN: 978-94-009-3051-3. DOI: `10.1007/978-94-009-3051-3_25`. [Online]. Available: `https://doi.org/10.1007/978-94-009-3051-3_25` (cit. on p. 1).

[9] S. Roesler, R. Engel, and J. Ranft, "The monte carlo event generator DPMJET-III," in *Advanced Monte Carlo for Radiation Physics, Particle Transport Simulation and Applications*, Springer Berlin Heidelberg, 2001. arXiv: `0012252 [hep-ph]` (cit. on pp. 11, 20).

[10] A. Kalweit, *Energy loss calibration of the ALICE TPC*, 2008 (cit. on p. 14).

[11] S. Acharya *et al.*, "Production of $\mathrm{K}^*(892)^0$ and $\phi(1020)$ in pp and p–Pb collisions at $\sqrt{s_{\mathrm{NN}}} = 5.02$ tev," *Phys. Rev.*, vol. C97, 2022. DOI: `10.1103/physrevc.106.034907`. [Online]. Available: `https://doi.org/10.1103%2Fphysrevc.106.034907` (cit. on p. 18).

[12] R. Brun *et al.*, *GEANT: Detector Description and Simulation Tool; Oct 1994*, ser. CERN Program Library. Geneva: CERN, 1993, Long Writeup W5013. DOI: `10.17181/CERN.MUHF.DMJ1`. [Online]. Available: `http://cds.cern.ch/record/1082634` (cit. on p. 20).